Impact of pupillary dilation on the efficacy of laser peripheral iridotomy

Anup D. Pant[1], Frederick Sebastian[2], Keyvan Khoiy[1], Rodolfo Repetto[3], Syril Dorairaj[4], Rouzbeh Amini[2,5]

[1]*Department of Biomedical Engineering, The University of Akron, Akron, OH, USA*, [2]*Department of Bioengineering, Northeastern University, Boston, MA, USA*, [3]*Department of Civil, Chemical and Environmental Engineering, Universita degli Studi di Genova, Genova, Liguria, Italy*, [4]*Department of Ophthalmology, Mayo Clinic, Jacksonville, FL, USA*, [5]*Department of Mechanical and Industrial Engineering, Northeastern University, Boston, MA, USA*

Abstract

Purpose: To assess outcomes of laser peripheral iridotomy (LPI) procedures following dilation by evaluating the pressure difference across the iris posterior-anterior chamber resulting from varying hole sizes and locations.

Methods: Using an anterior segment optical coherence tomography (AS-OCT) image, we created a 3-D finite element model of the iris. We then manually identified a dilator region where the dilator stress was applied to simulate pupillary dilation. To mimic LPI, we made a hole of 200 microns in diameter near the pupillary margin, at the mid-periphery, and at the periphery of the iris. Using computational fluid dynamics methods, we computed the pressure difference developed by the hole before and after pupil dilation at each location. This process was then repeated with a hole of 400 microns in diameter.

Results: The pressure difference developed across a 200-micron hole when the hole was placed near the pupil, at the iris mid-periphery, and near the iris periphery was 0.85 Pa, 0.80 Pa, and 0.92 Pa, respectively. Following pupil dilation, the pressure difference increased in all cases. For the compressible iris model, the pressure increased

Correspondence: Rouzbeh Amini, Department of Mechanical and Industrial Engineering, Department of Bioengineering, Northeastern University, Boston, MA 02115, USA.
E-mail: r.amini@northeastern.edu

by 4.70%, 63.75%, and 52.17% near the pupil, at the iris mid-periphery, and near the iris periphery, respectively. For the nearly incompressible model, the pressure increased by 7.06%, 51.25%, and 55.43% near the pupil, at the iris mid-periphery, and near the iris periphery, respectively. Across a 400-micron diameter hole, the pressure difference developed was extremely small (< 0.1 Pa) across all cases, both before and following dilation.

Conclusion: While LPI offers a solution for narrow or closed anterior chamber angles, in some patient populations the angles remain occludable following LPI. One possible reason could be attributed to the additional pressure difference across the anterior and posterior chamber due to the change in LPI hole size following dilation-induced iris deformation. Our study shows that the LPI hole size/location affects the pressure difference in both compressible and nearly incompressible irides.

Keywords: angle closure, finite element model, glaucoma, iris, laser peripheral iridotomy

1. Introduction

Laser peripheral iridotomy (LPI) is a surgical technique in which a laser is used to create small holes in the iris of patients with narrow or closed anterior chamber angles (ACAs). LPI remains a common treatment method for pupillary block,[1] as it provides an alternative pathway for the aqueous humor (AH) to flow into the anterior chamber, equalizing the pressure difference between the anterior and posterior chambers and thus flattening the iris.

Nevertheless, the long-term effectiveness of the LPI procedure remains uncertain. Research indicates that patients who have undergone LPI often experience significant increases in intraocular pressure (IOP). Consequently, many require further treatments, including filtering procedures, to manage these effects over time.[2,3] Additionally, researchers have found the success rate of LPI to be as low as 24%.[4,5] Furthermore, we have also shown that some patients who underwent LPI and continued to present with occludable ACAs had stiffer irides, indicating the importance of biomechanical factors in the success of the LPI procedure.[6] Hole sizes of at least 150–200 microns in diameter have been advocated for the LPI procedure.[7] However, even among highly experienced clinicians, there is no unanimous agreement on the precise size and location of the LPI hole. Depending on their experience and judgment, they may choose a size ranging from 50 microns to 250 microns.[8] Consequently, the precise location and size of the LPI hole continue to be the subject of ongoing research.[9,10]

Computational models have been effectively utilized to illuminate the biomechanics of the iris and AH, both in understanding the normal functioning of the eye and in studying the pathophysiology of angle-closure glaucoma.[6,9–25] Employing similar computational methods, Dvoriashyna et al. demonstrated how pupillary block can be alleviated through the LPI hole, examining the influence of its size and location on AH pressure dynamics.[9] In parallel, Cai and colleagues investigated AH flow through the LPI in the anterior eye using a comparable computational framework.[10] Both studies underscore the critical role of the location and size of LPI in patients who suffer from closed or narrow ACAs. However, a notable limitation in these analyses is the assumption that the iris behaves passively. Contrary to this assumption, our work and that of other researchers has shown that iris contraction markedly alters its configuration.[6,13,17,19] As such, in this study, we hypothesized that iris deformation, triggered by contraction of its dilator muscle, could significantly modify the LPI hole and its subsequent effect on AH pressure. To explore this hypothesis, we employed anterior segment optical coherence tomography (AS-OCT) images and computer-aided simulations to model post-LPI iris behavior. We aimed to re-evaluate the impact of LPI hole location and size, particularly focusing on how iris dilation may influence LPI outcomes.

2. Methods

2.1 Three-dimensional modeling of the iris

A three-dimensional (3-D) model of the iris was constructed using an AS-OCT (Carl Zeiss Meditec, Inc., Dublin, CA, USA) image captured from the eye of a 59-year-old healthy female subject from the LV Prasad Eye Institute in Hyderabad, India. This study followed the ethical principles outlined in the Declaration of Helsinki.[6]

The 3-D model was generated by revolving the 2-D iris image around the corneal axis, as shown in Figure 1. A corresponding dilator region was manually assigned to the model (Fig. 1A). To simulate LPI, a hole with a specific diameter was placed in the iris (Fig. 2). Finite element meshes of the iris were constructed using Abaqus (Dassault Systèmes, Velizy-Villacoublay, France) using tetrahedral elements (Fig. 2C,D).

2.2 Governing equation

The iris was modeled as a hyper-elastic solid material governed by the equations of the balance of the linear momentum in a quasi-static deformation manner:

$$\nabla \cdot \boldsymbol{\sigma} = 0 \tag{1}$$

with $\boldsymbol{\sigma}$ representing the Cauchy stress tensor. The Cauchy stress tensor was defined by neo-Hookean $\boldsymbol{\sigma}_{\mathrm{NH}}$ and active dilator $\boldsymbol{\sigma}_{\mathrm{D}}$ stress tensors:
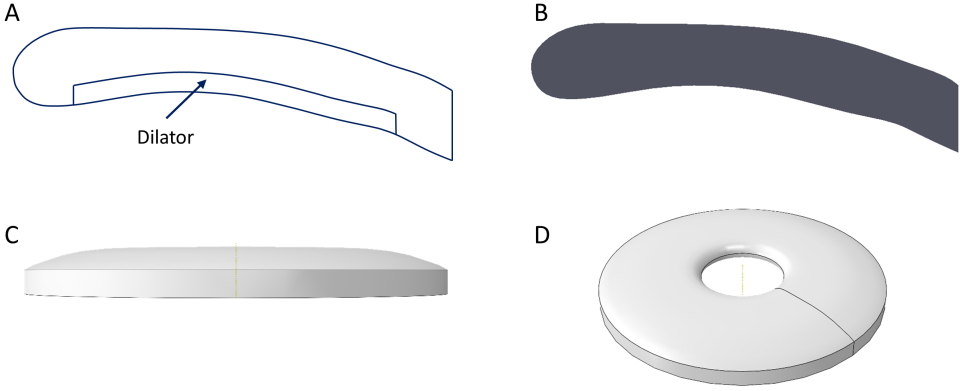
Fig. 1. Generation of the 3-D model of the iris: *(A)* 2-D sketch of the iris, *(B)* solid model of the iris, *(C)* 3-D geometry of the iris, and *(D)* isometric view of the 3-D geometry of the iris.

$$\boldsymbol{\sigma} = \boldsymbol{\sigma}_{\text{NH}} + \boldsymbol{\sigma}_{\text{D}} \tag{2}$$

The neo-Hookean stress was defined by:

$$\boldsymbol{\sigma}_{\text{NH}} = \frac{G}{\det\mathbf{F}}(\mathbf{B} - \mathbf{I}) + \frac{2G\nu}{(1 - 2\nu)\det\mathbf{F}}\ln(\det\mathbf{F})\mathbf{I} \tag{3}$$

where G is the shear modulus, ν is the Poisson's ratio, $\mathbf{I}$ is the identity tensor, det indicates the determinant of a tensor, $\mathbf{F}$ is the deformation gradient tensor, and $\mathbf{B}$ is the left Cauchy–Green deformation tensor. The tensors $\mathbf{F}$ and $\mathbf{B}$ are defined as:

$$\mathbf{F} = \frac{d\mathbf{x}}{d\mathbf{X}} \tag{4}$$

$$\mathbf{B} = \mathbf{F}\mathbf{F}^{T} \tag{5}$$

where $\mathbf{x}$ is the current position of a material point and $\mathbf{X}$ is its resting position. The dilator stress was defined by σ_{Act}, the scalar active muscle contraction stress, and $\mathbf{e}_d$, the unit vector representing the direction of the deformed dilator muscle:

$$\boldsymbol{\sigma}_{\text{D}} = \sigma_{\text{Act}}\mathbf{e}_d \otimes \mathbf{e}_d \tag{6}$$

where $\otimes$ indicates the tensor product of 2 vectors. The unit vector $\mathbf{e}_d$ was calculated as the product of the deformation gradient $\mathbf{F}$ and the unit vector $\mathbf{e}_d^o$ representing the direction of the undeformed dilator muscle.
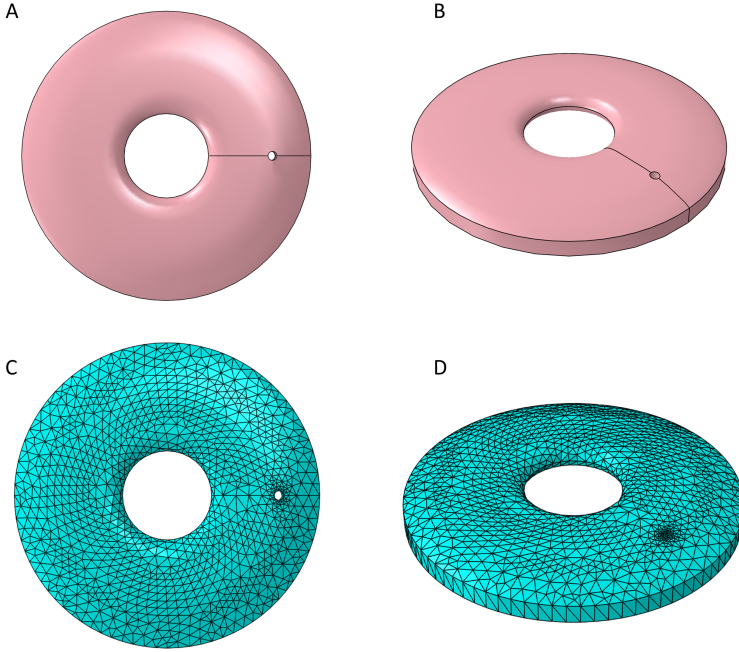
Fig. 2. An iris with a hole in it: *(A, B)* 3-D model; *(C, D)* finite element mesh.

$$\mathbf{e}_d = \mathbf{F}\mathbf{e}_d^o \tag{7}$$

For all simulated cases, 30 kPa was chosen as the magnitude of the active muscle contraction stress, σ_{Act}. This constant value was selected to solely simulate pupillary dilation and focus on LPI hole deformation during dilation. While this simplifies the model, future work could incorporate dynamic factors to represent physiological conditions more accurately, as described by Taber.[26]

2.3 Numerical solution

An internally developed computer code using C was employed to apply the Galerkin finite element method for spatial discretization of the mathematical model along the meshes generated.[16–19,27] The Newton-Raphson iteration and the direct linear solver MUltifrontal Massively Parallel sparse direct Solver (MUMPS; University of Bordeaux, Bordeaux, Nouvelle-Aquitaine, France) were employed in solving the nonlinear algebraic equations.[28]

2.4 Parametric analysis

Three modeling parameters were perturbed to examine the changes in the pressure difference between the posterior and anterior chambers as described below.

1. *The effect of hole location:* For this case, holes were placed in the iris at locations adjacent to the pupil, near the middle of the iris, and near the periphery of the iris (Figs. 3, 4).

2. *The effect of the hole size:* Holes with diameters of 200 microns and 400 microns were used to calculate the pressure difference (Figs. 3, 4).

3. *The effect of iris compressiblity:* Poisson's ratios of 0.35 (compressible) and 0.49 (nearly incompressible) were used to calculate the pressure difference.

It is worth noting that we used a Poisson's ratio of 0.49 to represent the nearly incompressible behavior of the iris, consistent with our previous work.[19] Alternatively, iris incompressibility can be modeled by introducing a Lagrange multiplier into the constitutive equations—as demonstrated in our studies in the iris,[16] or those of others in nonlinear tissues and man-made materials,[29–31] though this approach applies specifically to fully incompressible tissues.
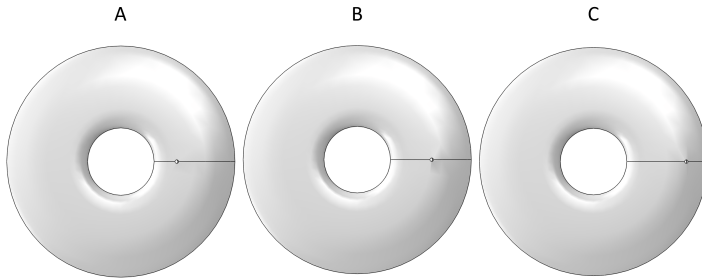

Fig. 3. Holes with a diameter of 200 microns placed *(A)* near the pupil, *(B)* in the central portion of the iris, and *(C)* near the periphery of the iris.

2.5 Computational fluid dynamics analysis of the hole shape

After obtaining the deformed configuration of the iris following finite element simulation (as shown in Fig. 5), the subsequent shape of the hole was analyzed. A comparison was performed between the initial shape of the hole and the deformed shape of the hole using computational fluid dynamics simulation (Fig. 6).

To determine the type of fluid flow, the Reynolds number was calculated first. Considering the flow of AH through the LPI hole as a pipe/tube flow, the Reynolds number
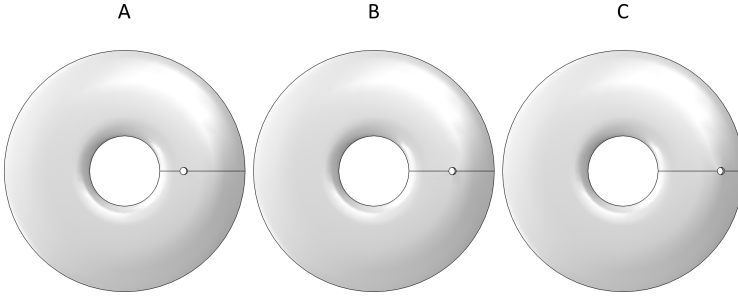
Fig. 4. Holes with a diameter of 400 microns placed *(A)* near the pupil, *(B)* in the central portion of the iris, and *(C)* near the periphery of the iris.
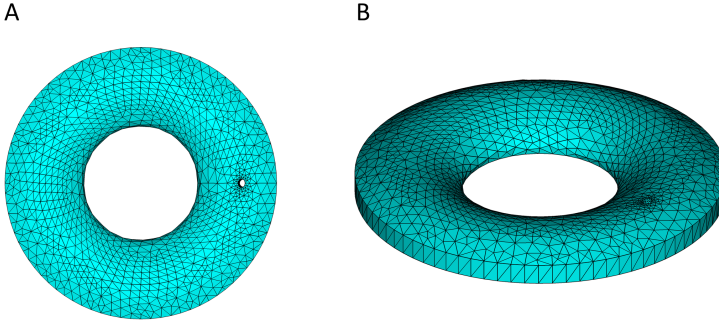

Fig. 5. Deformation of the iris following simulated pupillary dilation.

was calculated as:

$$Re = \frac{\rho v d}{\mu} \tag{8}$$

where ρ is the density of the fluid, v is the velocity, d is the diameter of the hole, and μ is the viscosity of the fluid.

In terms of the flow rate the volumetric flow rate Q, the equation can be written as:

$$Re = \frac{\rho Q d}{\mu A} \tag{9}$$

where A is the cross-sectional area of the hole. The flow rate Q was assumed to be 3.0 μL/min (5 x 10^{-11} m^3/s),[32] representing the "worst case scenario" in which all fluid flow occurs through the LPI, with negligible flow through the iris lens channel. This assumption justifies our efforts to improve the flow rate, Q, and compute the pressure drop. Additionally, it is worth noting that for Q, we use the aqueous production rate. The density and viscosity of AH were considered 1000 kg/m^3,[33] and 10^{-3}
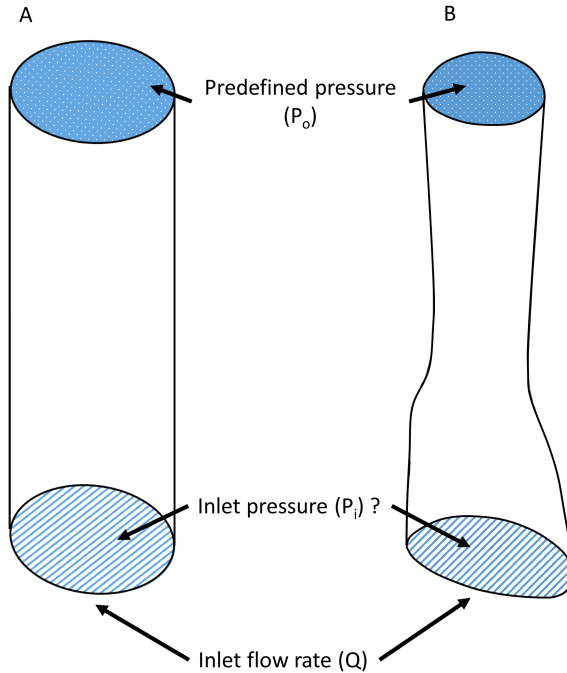
Fig. 6. Boundary conditions applied to the undeformed and deformed hole for computational fluid dynamics analysis.

kg/m.s,[34] respectively. Substituting these parameter values, the Reynolds number was calculated to be 0.3; therefore, the AH flow through the LPI hole was considered to be laminar.

The geometry of the hole before and after dilation was imported into SolidWorks (Fig. 6) and a flow simulation was performed using the Flow Simulation add-in in Solidworks (Dassault Systèmes, Velizy-Villacoublay, France). For the boundary conditions, the inlet surface of the hole had a volumetric flow rate of 3.0 μL/min (5 x 10^{-11} m^3/s),while the outlet surface was set to a pressure value of 0 (Fig. 6). Thus, the pressure difference required to drive the flow the fluid through the hole could be calculated. This choice was made to provide a reference point for calculating the pressure difference driving the flow and does not directly correspond to physiological or pathological IOP ranges. The pressure difference between the 2 ends of the hole before and after dilation was calculated.

3. Results

Figure 7 and Figure 8 show the relative pressure distribution along the hole for an LPI hole diameter of 200 microns placed in the center of a compressible iris before and after dilation, respectively.
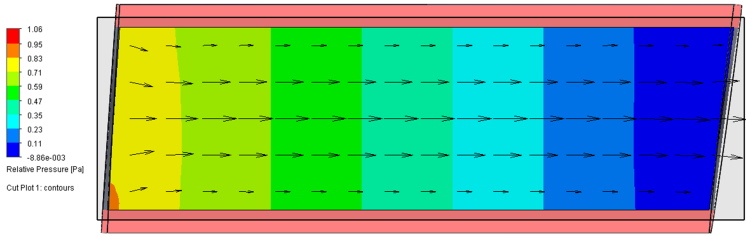

Fig. 7. Relative pressure difference across the hole ends and the flow profile for an undeformed hole.
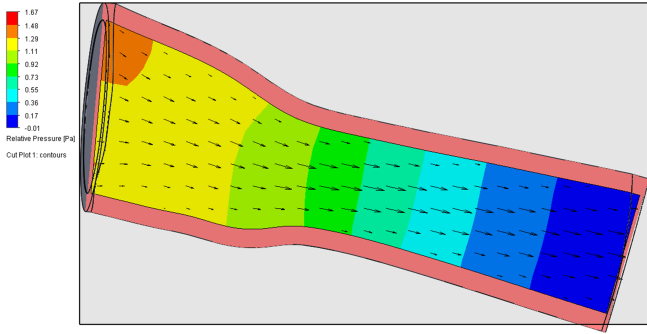

Fig. 8. Relative pressure difference across the hole ends and the flow profile for a deformed hole.

The pressure difference across the hole for the abovementioned cases are presented in Tables 1 to 4. Additionally, to investigate the pressure variation before and after dilation, the iris thickness in the proximity of the holes was also measured. The thickness measurement results from model outputs are presented in Tables 5 and 6.

4. Discussion

To our knowledge, we have illustrated for the first time the impact of iris dilator muscle contraction on the hole created by the LPI procedure. Our findings reveal how

Table 1. Effect of hole location on the pressure difference using a hole diameter of 200 microns for a compressible ($\nu = 0.35$) case.

Location	Pre-LPI pressure difference (Pa)	Post-LPI pressure difference (Pa)
Near pupil	0.85	0.89
Center	0.80	1.31
Periphery	0.92	1.40

Table 2. Effect of hole location on the pressure difference using a hole diameter of 200 microns for a nearly incompressible ($\nu = 0.49$) case.

Location	Pre-LPI pressure difference (Pa)	Post-LPI pressure difference (Pa)
Near pupil	0.85	0.91
Center	0.80	1.21
Periphery	0.92	1.43

this contraction subsequently alters the pressure difference between the posterior and anterior chambers. For a 200-micron hole, we found that placing the hole in the center of the iris resulted in the least pressure difference across the hole ends before dilation. However, after dilation, the pressure difference was the least for a hole in the pupillary region. In addition to the hole location, the magnitude of the dilator muscle stress should also be taken into account when considering the results presented in this study. For instance, if the magnitude of the dilator muscle is greater and the hole indeed collapses to a greater extent as the pupillary dilation increases, one can be sure that the hole size will be considerably smaller as compared to those in this study. For a pipe flow, the pressure difference across the tube is inversely proportional to the fourth power of the diameter, which means that a 50% decrease in the hole diameter will increase the pressure difference by a factor of 16. As such, a more significant deformation in dilation may result in a smaller hole size and subsequently a much larger pressure difference between the 2 chambers.

In this study, we also calculated the pressure difference across the hole ends for a hole with a diameter of 400 microns. The results showed a considerably smaller pressure difference across the hole ends when compared to that for a hole that was 200 microns in diameter. While it may be tempting to use a large diameter for the hole, one should be cautious regarding the hole size. A large hole size may cause the formation of a secondary pupil, thereby altering the eye's normal optics.

We found that, as expected, the pressure difference was directly proportional to the thickness, so a thicker iris would have a larger pressure drop across the hole ends as compared to a thinner iris. Therefore, the thickness of the iris should also be taken into consideration when performing LPI. Our model further demonstrates that iris

Table 3. Effect of hole location on the pressure difference using a hole diameter of 400 microns for a compressible ($\nu = 0.35$) case.

Location	Pre-LPI pressure difference (Pa)	Post-LPI pressure difference (Pa)
Near pupil	0.05	0.05
Center	0.05	0.07
Periphery	0.06	0.08

Table 4. Effect of hole location on the pressure difference using a hole diameter of 400 microns for a nearly incompressible ($\nu = 0.49$) case.

Location	Pre-LPI pressure difference (Pa)	Post-LPI pressure difference (Pa)
Near pupil	0.05	0.05
Center	0.05	0.08
Periphery	0.06	0.09

thickness tends to increase slightly as Poisson's ratio (ν) approaches 0.5, particularly at the iris periphery, reflecting the near incompressibility of biological tissues. The saturation of iris thickness with increasing ν depends on both the hole size and location, with larger and more peripheral holes showing greater deformations. This behavior contributes to a larger pressure differential across the LPI hole. The predicted lower pressure difference for thinner irides was consistent with the clinical studies reporting higher rate of LPI success for this cohort.[35]

In this study, we employed a unified geometry to establish our model domain, drawing on mechanical properties of the iris as documented in existing literature. While this modeling approach served our initial purposes, it harbors the capability for patient-specific analyses, provided that detailed anatomical specifications and mechanical characteristics of individual patients are accessible. Through the precise quantification of the dilator region, facilitated by advanced imaging techniques as well as the measurement of stiffness and Poisson's ratio, constructing accurate iris models becomes feasible.[21] Such models have the potential to predict LPI procedure outcomes on a case-by-case basis.

Using AS-OCT has proven valuable in assessing pre- and post-LPI outcomes, as highlighted by Koh et al.[36] In their study, specific anatomical parameters such as iris concavity, angle recess area, and iris thickness were used to predict LPI success with approximately 80% accuracy. This underscores the potential for using patient-specific data to guide clinical decisions. By incorporating such AS-OCT features into our computational framework, we can extend our model to predict the optimal size and location for LPI based on individual anatomy. This personalized approach would enable clinicians to tailor treatments more effectively, improving LPI outcomes by

Table 5. Iris thickness measurement for a 200-micron hole in LPI. Poisson's ratio (ν) is set at 0.35 and 0.49 for compressible and nearly incompressible iris, respectively.

Location	Undeformed thickness (mm)	Deformed thickness (mm) for ν = 0.35	Deformed thickness (mm) for ν = 0.49
Near pupil	0.72	0.72	0.73
Center	0.68	0.75	0.77
Periphery	0.75	0.82	0.85

Table 6. Iris thickness measurement for a 400-micron hole in LPI. Poisson's ratio (ν) is set at 0.35 and 0.49 for compressible and nearly incompressible iris, respectively.

Location	Undeformed thickness (mm)	Deformed thickness (mm) for ν = 0.35	Deformed thickness (mm) for ν = 0.49
Near pupil	0.74	0.73	0.73
Center	0.69	0.76	0.78
Periphery	0.75	0.81	0.84

addressing patient-specific anatomical differences.

Our study is not without limitations. We made assumptions regarding dilator muscle location. Moreover, the dilator muscular stress may not necessarily be an exact representation of the human eye. However, since these assumptions were consistent among all our case studies, comparative results presented here can be confidently assumed. We showed that even with a small variation in the location of the LPI holes, a measurable pressure difference was developed across the hole ends.

5. Educational component

In our recent publications,[37–46] we have incorporated educational elements to enhance the reach and influence of our research. Similarly, the "homework problem" outlined below is designed to assist students in evaluating their understanding of fluid flow through a cylindrical hole, following their engagement with the research section of the manuscript. This task is designed for students enrolled in an introductory undergraduate bio-transport or fluid mechanics course.

Problem

In this study, we simulated holes measuring 200 and 400 microns in diameter. However, holes as small as 50 microns are also used clinically.[8] Assuming Poiseuille flow,[47] one could estimate that the pressure drop across the hole is inversely proportional to the fourth power of its radius, given a constant flow rate. Utilizing the data from pre-LPI cases, find an approximation for the pressure drop of an LPI hole with a diameter of 50 microns.

Declarations

Ethics approval and consent to participate

This study was conducted in accordance with the Declaration of Helsinki.

Competing interests

None to declare.

References

1. Laser Peripheral Iridotomy for Pupillary-block Glaucoma. Ophthalmology, 1994;101(10): 1749–1758. ISSN: 0161-6420. Available from: https : / / www . sciencedirect . com / science / article / pii / S0161642013314341. doi: https://doi.org/10.1016/S0161-6420(13)31434-1.

2. Aung T, Ang LP, Chan SP, Chew PT. Acute primary angle-closure: long-term intraocular pressure outcome in Asian eyes. American Journal of Ophthalmology, 2001;131(1): 7–12. ISSN: 0002-9394. Available from: https://www.sciencedirect.com/science/article/pii/S0002939400006218. doi: https://doi.org/10.1016/S0002-9394(00)00621-8.

3. Alsagoff Z, Aung T, Ang LP, Chew PT. Long-term clinical course of primary angle-closure glaucoma in an Asian population. Ophthalmology, 2000;107(12): 2300–2304. ISSN: 0161-6420. Available from: https://www.sciencedirect.com/science/article/pii/S0161642000003857. doi: https://doi.org/10.1016/S0161-6420(00)00385-7.

4. Han S, Sung KR, Lee KS, Hong JW. Outcomes of Laser Peripheral Iridotomy in Angle Closure Subgroups According to Anterior Segment Optical Coherence Tomography Parameters. Investigative Ophthalmology & Visual Science, 2014;55(10): 6795–6801. ISSN: 1552-5783. doi: 10.1167/iovs.14-14714.

5. Rao A, Rao HL, Kumar AU, Babu JG, Madhulata U, Arthi J, et al. Outcomes of Laser Peripheral Iridotomy in Angle Closure Disease. Seminars in Ophthalmology, 2013;28(1): 4–8. doi: 10.3109/08820538.2012.702260.

6. Pant AD, Gogte P, Pathak-Ray V, Dorairaj SK, Amini R. Increased Iris Stiffness in Patients With a History of Angle-Closure Glaucoma: An Image-Based Inverse Modeling Analysis. Investigative Ophthalmology & Visual Science, Aug. 2018;59(10): 4134–4142. ISSN: 1552-5783. doi: 10.1167/iovs.18-24327.

7. Fleck BW. How large must an iridotomy be? British Journal of Ophthalmology, 1990;74(10): 583–588. ISSN: 0007-1161. Available from: https://bjo.bmj.com/content/74/10/583. doi: 10.1136/bjo.74.10.583.

8. Asrani S, Foster P, Palmberg P, R R. MD Roundtable: Iridotomy Decisions for the Narrow Angle. https://www.aao.org/eyenet/article/md-roundtable-iridotomy-decisions-narrow-angle. Accessed: 2023-11-07. 2015;

9. Dvoriashyna M, Repetto R, Romano M, Tweedy J. Aqueous humour flow in the posterior chamber of the eye and its modifications due to pupillary block and iridotomy. Mathematical medicine and biology: a journal of the IMA, 2018;35(4): 447–467.

10. Cai JC, Chen YL, Cao YH, Babenko A, Chen X. Numerical study of aqueous humor flow and iris deformation with pupillary block and the efficacy of laser peripheral iridotomy. Clinical Biomechanics, 2022;92, 105579.

11. Heys JJ, Barocas VH, Taravella MJ. Modeling passive mechanical interaction between aqueous humor and iris. Journal of Biomechanical Engineering, 2001;123(6): 540–547.

12. Heys JJ, Barocas VH. Computational evaluation of the role of accommodation in pigmentary glaucoma. Investigative ophthalmology & visual science, 2002;43(3): 700–708.

13. Huang EC, Barocas VH. Active iris mechanics and pupillary block: steady-state analysis and comparison with anatomical risk factors. Annals of biomedical engineering, 2004;32(9): 1276–1285.

14. Huang EC, Barocas VH. Accommodative microfluctuations and iris contour. Journal of Vision, 2006;6(5): 10–10.

15. Amini R, Barocas VH. Anterior chamber angle opening during corneoscleral indentation: the mechanism of whole eye globe deformation and the importance of the limbus. Investigative ophthalmology & visual science, 2009;50(11): 5288–5294.

16. Amini R, Barocas VH. Reverse Pupillary Block Slows Iris Contour Recovery From Corneoscleral Indentation. Journal of Biomechanical Engineering, May 2010;132(7): 071010. ISSN: 0148-0731. doi: 10.1115/1.4001256.

17. Amini R, Whitcomb JE, Al-Qaisi MK, Akkin T, Jouzdani S, Dorairaj S, et al. The Posterior Location of the Dilator Muscle Induces Anterior Iris Bowing during Dilation, Even in the Absence of Pupillary Block. Investigative Ophthalmology & Visual Science, Mar. 2012;53(3): 1188–1194. ISSN: 1552-5783. doi: 10.1167/iovs.11-8408.

18. Amini R, Jouzdani S, Barocas VH. Increased iris–lens contact following spontaneous blinking: Mathematical modeling. Journal of Biomechanics, 2012;45(13): 2293–2296. ISSN: 0021-9290. Available from: https://www.sciencedirect.com/science/article/pii/S0021929012003508. doi: https://doi.org/10.1016/j.jbiomech.2012.06.018.

19. Jouzdani S, Amini R, Barocas VH. Contribution of Different Anatomical and Physiologic Factors to Iris Contour and Anterior Chamber Angle Changes During Pupil Dilation: Theoretical Analysis. Investigative Ophthalmology & Visual Science, Apr. 2013;54(4): 2977–2984. ISSN: 1552-5783. doi: 10.1167/iovs.12-10748.

20. Repetto R, Pralits JO, Siggers JH, Soleri P. Phakic iris-fixated intraocular lens placement in the anterior chamber: effects on aqueous flow. Investigative ophthalmology & visual science, 2015;56(5): 3061–3068.

21. Pant AD, Dorairaj SK, Amini R. Appropriate Objective Functions for Quantifying Iris Mechanical Properties Using Inverse Finite Element Modeling. Journal of Biomechanical Engineering, Apr. 2018;140(7): 074502. ISSN: 0148-0731. doi: 10.1115/1.4039679.

22. Wang W, Song H, Liu Z, et al. Computational study on the biomechanics of pupil block phenomenon. BioMed Research International, 2019;2019.

23. Thomas VS, Salinas SD, Pant AD, Dorairaj SK, Amini R. Biomechanical assessment of the Iris in relation to angle-closure glaucoma: a multi-scale computational approach. Computer Methods, Imaging and Visualization in Biomechanics and Biomedical Engineering: Selected Papers from the 16th International Symposium CMBBE and 4th Conference on Imaging and Visualization, August 14-16, 2019, New York City, USA. Springer. 2020; 470–482.

24. Lee C, Li G, Stamer WD, Ethier CR. In vivo estimation of murine iris stiffness using finite element modeling. Experimental eye research, 2021;202, 108374.

25. Safa B, Fraticelli Guzmán NS, Li G, Stamer D, Feola A, Ethier CR. A Histomorphometric and Computational Investigation of the Stabilizing Role of Pectinate Ligaments in the Aqueous Outflow Pathway. Journal of Biomechanical Engineering, Mar. 2024; 1–43. ISSN: 0148-0731. eprint: https :

//asmedigitalcollection.asme.org/biomechanical/article- pdf/doi/10.1115/1.4065164/7322638/bio-23-1388.pdf. Available from: https://doi.org/10.1115/1.4065164. doi: 10.1115/1.4065164.

26. Taber LA. Continuum modeling in mechanobiology. 10. Springer, 2020;

27. Pant AD, Kagemann L, Schuman JS, Sigal IA, Amini R. An imaged-based inverse finite element method to determine in-vivo mechanical properties of the human trabecular meshwork. Journal for Modeling in Ophthalmology, 2017;1(3): 100–111. Available from: https://www.ncbi.nlm.nih.gov/pmc/articles/PMC5766041/.

28. Amestoy P, Duff I, L'Excellent JY. Multifrontal parallel distributed symmetric and unsymmetric solvers. Computer Methods in Applied Mechanics and Engineering, 2000;184(2): 501–520. ISSN: 0045-7825. Available from: https://www.sciencedirect.com/science/article/pii/S004578259900242X. doi: https://doi.org/10.1016/S0045-7825(99)00242-X.

29. Shariff M. An extension of Herrmann's principle to nonlinear elasticity. Applied Mathematical Modelling, 1997;21(2): 97–107.

30. Weiss JA, Maker BN, Govindjee S. Finite element implementation of incompressible, transversely isotropic hyperelasticity. Computer methods in applied mechanics and engineering, 1996;135(1-2): 107–128.

31. Gasser TC, Ogden RW, Holzapfel GA. Hyperelastic modelling of arterial layers with distributed collagen fibre orientations. Journal of the royal society interface, 2006;3(6): 15–35.

32. Goel M, Picciani RG, Lee RK, Bhattacharya SK. Aqueous Humor Dynamics: A Review. The Open Ophthalmology Journal, 2010;4, 52. doi: 10.2174/1874364101004010052.

33. Scott JA. A Finite Element Model of Heat Transport in The Human Eye. Physics in Medicine & Biology, 1988;33(2): 227. doi: 10.1088/0031-9155/33/2/003.

34. Beswick JA, McCulloch C. Effect of Hyaluronidase on the Viscosity of the Aqueous Humour. British Journal of Ophthalmology, 1956;40(9): 545–548. ISSN: 0007-1161. doi: 10.1136/bjo.40.9.545.

35. Lee RY, Kasuga T, Cui QN, Porco TC, Huang G, He M, et al. Association between baseline iris thickness and prophylactic laser peripheral iridotomy outcomes in primary angle-closure suspects. Ophthalmology, 2014;121(6): 1194–1202.

36. Koh V, Keshtkaran MR, Hernstadt D, Aquino MCD, Chew PT, Sng C. Predicting the outcome of laser peripheral iridotomy for primary angle closure suspect eyes using anterior segment optical coherence tomography. Acta ophthalmologica, 2019;97(1): e57–e63.

37. Thomas VS, Lai V, Amini R. A computational multi-scale approach to investigate mechanically-induced changes in tricuspid valve anterior leaflet microstructure. Acta biomaterialia, 2019;94, 524–535. doi: 10.1016/j.actbio.2019.05.074.

38. Vargas AI, Tarraf SA, Fitzgibbons TP, Bellini C, Amini R. Biomechanical remodeling of the murine descending thoracic aorta during late-gestation pregnancy. Current Research in Physiology, July 2023; 100102. ISSN: 26659441. doi: 10.1016/j.crphys.2023.100102.

39. Clarin J, Dang D, Santos L, Amini R. Mechanical Characterization of Porcine Tricuspid Valve Anterior Leaflets Over Time: Applications to Ex Vivo Studies. ASME Open Journal of Engineering, Jan. 2023;2. ISSN: 2770-3495. doi: 10.1115/1.4062477.

40. Nwotchouang BST, Eppelheimer MS, Biswas D, Pahlavian SH, Zhong X, Oshinski JN, et al. Accuracy of cardiac-induced brain motion measurement using displacement-encoding with stimulated echoes (DENSE) magnetic resonance imaging (MRI): A phantom study. Magnetic resonance in medicine, 2021;85(3): 1237–1247.

41. Jennings T, Amini R, Müftü S. Toward a Consistent Framework for Describing the Free Vibration Modes of the Brain. Journal of Biomechanical Engineering, 2025;147(4):

42. Sebastian F, Vargas AI, Clarin J, Hurgoi A, Amini R. Meta Data Analysis of Sex Distribution of Study Samples Reported in Summer Biomechanics, Bioengineering, and Biotransport Annual Conference Abstracts. Journal of Biomechanical Engineering, 2024;146(6):

43. Jennings T, Tillman A, Mukasa D, Marchev M, Müftü S, Amini R. Measurement and Assessment of Head-to-Helmet Contact Forces. Annals of Biomedical Engineering, 2025; 1–10.

44. Pakzadmanesh M, Salinas SD, Thomas VS, Jennings T, DelCiello H, Vargas AI, et al. Mechanically in-duced deformation of nuclei in the tricuspid valve interstitial cells: experimental measurements and multi-scale computational simulation. ASME Open Journal of Engineering, 2024;3.

45. Sebastian F, DelCiello H, Pant AD, Girard MJ, Pathak-Ray V, Dorairaj SK, et al. Image-Based Inverse Modeling Analysis of Iris Stiffness Across Sex in Patients With a History of Primary Angle-Closure Dis-ease. ASME Open Journal of Engineering, 2025;4.

46. Vargas AI, Tarraf SA, Jennings T, Bellini C, Amini R. Vascular Remodeling During Late-Gestation Preg-nancy: An In-Vitro Assessment of the Murine Ascending Thoracic Aorta. Journal of Biomechanical En-gineering, Mar. 2024;146(7): 071004. ISSN: 0148-0731. Available from: https://doi.org/10.1115/1.4064744. doi: 10.1115/1.4064744.

47. Poiseuille JL. Recherches expérimentales sur le mouvement des liquides dans les tubes de très-petits diamètres. Imprimerie Royale, 1844;